Surface-peaked medium effects in the interaction of nucleons with finite nuclei

F. J. Aguayo[1,*] and H. F. Arellano[1,†]

[1] *Department of Physics - FCFM, University of Chile*
Av. Blanco Encalada 2008, Santiago, Chile

Abstract

We investigate the asymptotic separation of the optical model potential for nucleon-nucleus scattering in momentum space, where the potential is split into a medium-independent term and another depending exclusively on the gradient of the density-dependent g matrix. This decomposition confines the medium sensitivity of the nucleon-nucleus coupling to the surface of the nucleus. We examine this feature in the context of proton-nucleus scattering at beam energies between 30 and 100 MeV and find that the pn coupling accounts for most of this sensitivity. Additionally, based on this general structure of the optical potential we are able to treat both, the medium dependence of the effective interaction and the full mixed density as described by single-particle shell models. The calculated scattering observables agree within 10% with those obtained by Arellano, Brieva and Love in their momentum-space g-folding approach.

[*] Electronic address: faguayo@dfi.uchile.cl

[†] Electronic address: arellano@dfi.uchile.cl; URL: `http://www.omp-online.cl`

I. INTRODUCTION

Microscopic optical model potentials for nucleon-nucleus (NA) scattering are usually expressed as the convolution of a two-body effective interaction with the target ground-state mixed density. Their realization becomes feasible with the use of Brueckner-Bethe-Goldstone g matrices and resorting to simplifying assumptions in their coordinate and/or momentum dependence. Thus, nuclear medium effects are disclosed by means of volume integrals of density-dependent interactions throughout the nucleus[1, 2].

In this article we explore in more detail a recent finding suggesting that intrinsic nuclear medium effects, namely those arising from the dependence of the g matrix on the density, are dominantly localized in the nuclear surface, *i.e.* regions where the gradient of g is strongest [3]. This result is a consequence of a close examination of the momentum- and coordinate-space structure of a two-body effective interaction spherically symmetric in its mean coordinate. It is demonstrated quite generally that two-body interactions can be expressed as a non-trivial sum of a medium-independent term and another which is functionally –and exclusively– proportional to the gradient of the reduced *in-medium* interaction. As a result, the optical potential in momentum space becomes the sum of medium-free (free t matrix) and medium-dependent (g matrix) contributions, the latter depending exclusively on the variations of the effective interaction with respect to the mean coordinate. This feature yields an enhancement of the intrinsic medium effects in the nuclear surface and suppression in the saturated volume. We have investigated the manifestation of this selectivity in NA scattering at proton energies below 100 MeV, identifying major sensitivity in the pn couplings.

Current trends in nuclear research and applications have resulted in the development and construction of novel research facilities around the world. Such is the case of radioactive ion beam accelerators in the US, Europe and Japan [4, 5, 6, 7, 8], where intense rare isotope beams are produced and collided against selected targets. As the energy of these beams are projected to reach 500A MeV, their scattering from hydrogen targets would result equivalent to intermediate-energy proton collisions from an exotic nucleus. At energies below 60A MeV the collision would correspond to low-energy proton-nucleus scattering, a regime where the inclusion of medium effects in the effective interaction is known to be important. These unique facilities will expand our access to the neutron drip line from the region roughly below carbon isotopes to nuclei as heavy as ^{52}S, the most neutron-rich nucleus. Just before the neutron drip line is reached, neutrons occupy weakly bound states spread well away from the bulk of the nucleus. Hence, from the NA scattering point of view, counting on an approach capable of tracking more selectively the various contributions to the optical model potential –particularly its surface structure– could prove useful for studying and interpreting data from rare isotope beam facilities. In this article we present and investigate a simplified form of the unabridged optical model potential discussed in Ref. [3], paying attention to the surface structure which emerges from the intrinsic medium effects as implied by the theory. Additionally, this form allows us to treat explicitly the off-shell mixed density, a long standing limitation of the microscopic *in-medium* folding approach of Arellano, Brieva and Love (ABL) [9], where the Slater approximation is used.

This article is organized as follows. In Section II we outline the general framework, discuss the general structure of the optical model potential in the single scattering approximation, introduce the 'δg-folding' approach and make contact with known approximations. Additionally, we examine more closely the various contributions to the optical potential, their energy and density dependence. In Section III we present and discuss results from selected applications of proton elastic scattering at energies between 30 and 100 MeV. In Section IV we summarize this work and present its main conclusions.

II. THEORETICAL FRAMEWORK

From a broad perspective diverse formal expressions of the optical model potential for NA scattering can be found in the literature [10, 11, 12, 13, 14]. Although they may differ in the way contact is made with the bare NN potential, they all take the form of a ground-state expectation value of a generalized two-body interaction. Thus, a general representation of the optical model potential for collisions of nucleons with kinetic energy E off a composite target is given by

$$U(\boldsymbol{k}',\boldsymbol{k};E) = \int d\boldsymbol{p}'\, d\boldsymbol{p}\, \langle \boldsymbol{k}'\boldsymbol{p}' \mid \hat{T}(E) \mid \boldsymbol{k}\, \boldsymbol{p}\, \rangle_{\mathcal{A}}\, \hat{\rho}(\boldsymbol{p}',\boldsymbol{p})\ , \tag{1}$$

where the subscript $\mathcal{A}$ indicates antisymmetrization. In general, $\hat{T}$ contains information about the discrete spectrum of the many-body system. In this expression $\hat{\rho}(\boldsymbol{p}',\boldsymbol{p})$ represents the one-body mixed density corresponding to the ground-state of the target. A comprehensive evaluation of the optical potential considering the full $\hat{T}$ matrix would require the solution of the $(A+1)$-body system, a formidable challenge. This difficulty is circumvented by decoupling the two-body effective interaction from the ground-state structure, a suitable strategy at intermediate and high energies when the discrete spectrum of the many-body Green's function is away from the projectile energy in the continuum. This allows the use of single-particle models to describe the target ground state and the Brueckner-Bethe-Goldstone reaction matrix to represent the effective interaction.

A. Structure of the optical potential

As expressed in Eq. (1), a central element in the evaluation of the optical potential is the representation of the two-body effective interaction. Quite generally, regardless of the physics content or particular structure conceived for the *NN* interaction, the two-body operator $\hat{T}$ in coordinate space requires the specification of four vectors. This leads to matrix elements of the form $\langle \boldsymbol{r}'\boldsymbol{s}' \mid \hat{T} \mid \boldsymbol{r}\ \boldsymbol{s}\rangle$, where $\boldsymbol{r}$ and $\boldsymbol{s}$ denote the 'prior' coordinates of the projectile and target nucleon, respectively. The primed vectors refer to 'post' coordinates. With these definitions, the so called local coordinate $\boldsymbol{Z}$ (hereafter referred as the *mean coordinate*) becomes

$$\boldsymbol{Z} = \tfrac{1}{4}(\boldsymbol{r}' + \boldsymbol{r} + \boldsymbol{s}' + \boldsymbol{s})\ ,$$

corresponding to the simple average of the prior and post coordinates of the interacting pair.

As demonstrated in Ref. [3], the momentum-space representation of the $\hat{T}$ matrix can be cast in terms of a reduced interaction, $g_{\boldsymbol{Z}}$, in the form

$$\langle \boldsymbol{k}'\boldsymbol{p}' \mid \hat{T} \mid \boldsymbol{k}\ \boldsymbol{p}\rangle = \int \frac{d\boldsymbol{Z}}{(2\pi)^3}\, e^{i\boldsymbol{Z}\cdot(\boldsymbol{Q}-\boldsymbol{q})}\, g_{\boldsymbol{Z}}(\boldsymbol{K}_{\parallel};\boldsymbol{\kappa}',\boldsymbol{\kappa})\ . \tag{2}$$

In Eq. (2) $\boldsymbol{Q} = \boldsymbol{p}' - \boldsymbol{p}$, the recoil of the target nucleon; $\boldsymbol{q} = \boldsymbol{k} - \boldsymbol{k}'$, the momentum transfer of the projectile; $\boldsymbol{K} = (\boldsymbol{k} + \boldsymbol{k}')/2$, the mean momentum of the projectile; $\boldsymbol{P} = (\boldsymbol{p}' + \boldsymbol{p})/2$, the mean momentum of the struck nucleon; and

$$\boldsymbol{\kappa}' = \tfrac{1}{2}(\boldsymbol{k}' - \boldsymbol{p}') \ = \ \tfrac{1}{2}[\boldsymbol{K} - \boldsymbol{P} - \tfrac{1}{2}(\boldsymbol{q} + \boldsymbol{Q})]\ , \tag{3a}$$

$$\boldsymbol{\kappa} = \tfrac{1}{2}(\boldsymbol{k} - \boldsymbol{p}) \ = \ \tfrac{1}{2}[\boldsymbol{K} - \boldsymbol{P} + \tfrac{1}{2}(\boldsymbol{q} + \boldsymbol{Q})]\ , \tag{3b}$$

the post and prior relative momenta, respectively. Furthermore,

$$\boldsymbol{K}_{\parallel} = \boldsymbol{K} + \boldsymbol{P} = \tfrac{1}{2}(\boldsymbol{k} + \boldsymbol{k}' + \boldsymbol{p} + \boldsymbol{p}')\ , \tag{4}$$

interpreted as a longitudinal momentum of the interacting nucleons [3]. With these definitions the integrals on $(\boldsymbol{p},\boldsymbol{p}')$ in Eq. (1) are accounted for by $(\boldsymbol{P},\boldsymbol{Q})$, with $d\boldsymbol{p}'d\boldsymbol{p}=d\boldsymbol{Q}\,d\boldsymbol{P}$.

What is interesting about the above representation for $\hat{T}$ is that it prescribes naturally the way the medium dependence of the two-body interaction is mapped through the mean coordinate $\boldsymbol{Z}$ in the reduced interaction. To model this dependence we have resorted to infinite nuclear matter, a reasonable starting point to incorporate leading-order correlations in the nuclear medium. In this approach, to each coordinate $\boldsymbol{Z}$ we associate its nuclear isoscalar density $\rho(\boldsymbol{Z})=[\rho_n(Z)+\rho_p(Z)]/2$, therefore a symmetric nuclear matter Brueckner-Bethe-Goldstone reaction matrix $g_{\boldsymbol{Z}}$ (g matrix) satisfying

$$\hat{g}(\Omega)=\hat{v}+\hat{v}\,\frac{\hat{Q}}{\Omega+i0-\hat{h}_1-\hat{h}_2}\,\hat{g}(\Omega)\;. \tag{5}$$

Here $\hat{v}$ is the bare NN potential, $\hat{h}_1$ and $\hat{h}_2$ the quasi-particle energies at density ρ, and $\hat{Q}$ the Pauli blocking operator to suppress occupied intermediate states. The corresponding Fermi momentum is given by

$$k_F=(3\pi^2\rho)^{1/3}\;. \tag{6}$$

In a finite system, namely a system with confined matter distribution, we demand that $\lim_{Z\to\infty}\rho(\boldsymbol{Z})=0$, so that

$$\lim_{Z\to\infty}\,\hat{g}_{\boldsymbol{Z}}(\Omega)=\hat{t}(\Omega)\;, \tag{7}$$

the free-space t matrix.

In the context of a spherically symmetric matter distribution, the $\boldsymbol{Z}$ integral in Eq. (2) can be split in such a way that its asymptotic structure becomes isolated from the $\boldsymbol{Z}$-dependent term [3]. Accordingly

$$\langle\boldsymbol{k}'\boldsymbol{p}'\mid\hat{T}\mid\boldsymbol{k}\,\boldsymbol{p}\rangle=\delta(\boldsymbol{Q}-\boldsymbol{q})\,t(\boldsymbol{K}_{\|};\boldsymbol{\kappa}',\boldsymbol{\kappa})-\frac{1}{2\pi^2}\int_0^\infty Z^3dZ\;\Phi_1(Z\mid\boldsymbol{Q}-\boldsymbol{q}\mid)\,\frac{\partial g_Z}{\partial Z}\;, \tag{8}$$

where the momentum dependence of $\partial g_Z/\partial Z$ on $\boldsymbol{K}_{\|}$, $\boldsymbol{\kappa}'$ and $\boldsymbol{\kappa}$ is implicit. Here $\Phi_1(t)=j_1(t)/t$, with j_1 the spherical Bessel function of order 1. This profile function favors the recoil of the struck nucleon around $\boldsymbol{Q}\approx\boldsymbol{q}$, namely $\boldsymbol{k}+\boldsymbol{p}\approx\boldsymbol{k}'+\boldsymbol{p}'$. We observe that total momentum conservation can only be possible when the system exhibits translational invariance, as expressed when $\partial g_Z/\partial Z=0$.

Upon substitution of $\hat{T}$ from Eq. (8) into Eq. (1) for the optical potential we obtain

$$U=U_0+U_1\;, \tag{9}$$

with

$$U_0(\boldsymbol{k}',\boldsymbol{k};E) \;=\; \int d\boldsymbol{P}\;\hat{\rho}(\boldsymbol{q};\boldsymbol{P})\;t(\boldsymbol{K}_{\parallel};\boldsymbol{\kappa}',\boldsymbol{\kappa})\;; \tag{10a}$$

$$U_1(\boldsymbol{k}',\boldsymbol{k};E) \;=\; \frac{1}{2\pi^2}\int d\boldsymbol{Q}\;d\boldsymbol{P}\;\hat{\rho}(\boldsymbol{Q};\boldsymbol{P})\;\times \int_0^\infty Z^3 dZ\;\Phi_1(Z|\boldsymbol{Q}-\boldsymbol{q}|)\left(-\frac{\partial g_Z}{\partial Z}\right)\;. \tag{10b}$$

The first term, U_0, depends exclusively on the medium-free reduced matrix, whereas the second depends on the gradient of the g matrix. In these expressions $\hat{\rho}$ denotes the full mixed-density, which in terms of occupied single-particle states ϕ_α is given by

$$\hat{\rho}(\boldsymbol{Q};\boldsymbol{P}) \equiv \sum_\alpha \hat{\rho}_\alpha(\boldsymbol{Q};\boldsymbol{P}) = \sum_\alpha \phi_\alpha^\dagger(\boldsymbol{p}')\,\phi_\alpha(\boldsymbol{p})\;.$$

Eq. (9) for U represents the most general expression to be given to the optical model potential when the two-body effective interaction exhibits spherical symmetry in the mean coordinate $\boldsymbol{Z}$. It summarizes the medium dependence of a general two-body effective interaction, accounting for all phase-space configurations allowed by the one-body mixed density. The interaction is evaluated off-shell, with no assumptions regarding its local/nonlocal structure. Furthermore, it involves a sevenfold integral, sixfold in momentum space and an additional integration in coordinate space. Thus, its evaluation constitutes a very challenging task even for nowadays computational capabilities. In this work we circumvent this difficulty by introducing a simplifying assumption, within the *momentum-conserving approximation*, to be explained in the following subsection. A thorough assessment of this assumption and its implications in actual scattering processes may require the evaluation of the sevenfold optical potential itself.

B. Limit cases and the δg-folding

The general form of the optical potential expressed above leads naturally to the free t matrix and ABL folding approaches. For instance, if the effective interaction is taken as the (transitionally invariant) free t matrix, then U_1 vanishes and U becomes U_0, the free t-matrix full-folding optical model potential applied to intermediate-energy NA scattering [15, 16]. In this case the medium effects do not come from the effective interaction but from the Fermi motion of the struck nucleons, as allowed by the spread of the one-body mixed density.

The evaluation of the optical potential for a spherically symmetric system involves a 7-fold integral. In order to simplify this, we neglect the dependence of $\partial g_Z/\partial Z$ on $\boldsymbol{Q}$ by setting $\boldsymbol{Q} \to \boldsymbol{q}$ in the interaction. This change is designated as $g_Z \to g_Z^{(0)}$, so that

$$U_1 \approx \frac{1}{2\pi^2} \sum_\alpha \int_0^\infty Z^3 dZ \int d\boldsymbol{P}\, \Omega_\alpha(\boldsymbol{q}, \boldsymbol{P}; Z) \left(-\frac{\partial g_Z^{(0)}}{\partial Z} \right) , \tag{11}$$

with

$$\Omega_\alpha(\boldsymbol{q}, \boldsymbol{P}; Z) = \int d\boldsymbol{Q}\; \hat{\rho}_\alpha(\boldsymbol{Q}; \boldsymbol{P})\; \Phi_1(Z|\boldsymbol{Q} - \boldsymbol{q}|) \;.$$

Noting that $\boldsymbol{Q} \to \boldsymbol{q}$ expresses momentum conservation of the interacting pair in the g matrix ($\boldsymbol{k}+\boldsymbol{p} = \boldsymbol{k}'+\boldsymbol{p}'$), we find appropriate to refer to this as momentum-conserving approximation (MCA). The appealing feature of this result is that it enables a detailed treatment of the full-mixed density as obtained from single-particle shell models while accounting for the medium dependence in the g matrix. The following discussions are mainly focused on this structure of the optical potential, referred hereafter as 'δg-folding'.

As demonstrated in Ref. [3], the use of the Slater approximation within the MCA leads to the ABL potential

$$U_{ABL} = 4\pi \int_0^\infty Z^2 dZ\; j_0(qZ)\, \rho(Z)\; \langle g_Z^{(0)} \rangle \;, \tag{12}$$

where $\langle g_Z^{(0)} \rangle$ denotes the Fermi-motion integral

$$\langle g_Z^{(0)} \rangle = \int d\boldsymbol{P}\; S_F(P; Z)\, g_Z[\boldsymbol{K}_\parallel; \tfrac{1}{2}(\boldsymbol{K} - \boldsymbol{P} - \boldsymbol{q}), \tfrac{1}{2}(\boldsymbol{K} - \boldsymbol{P} + \boldsymbol{q})] \;,$$

with

$$S_F(P; Z) = \frac{1}{\frac{4}{3}\pi \hat{k}^3(Z)}\; \Theta[\hat{k}(Z) - P] \;.$$

This step-function sets bounds for the off-shell sampling of the g matrix at a distance Z from the center of the nucleus, $|\,\boldsymbol{P}\,| \leq \hat{k}(Z)$, with $\hat{k}(Z) = [3\pi^2 \rho(Z)]^{1/3}$. The above result for U_{ABL} can also be obtained by replacing directly the two-body effective interaction [c.f. Eq. (2)] into Eq. (1) for U, applying the MCA and representing the mixed density by its Slater form.

All the above forms of the optical potential are nonlocal, as a consequence of the momentum structure of the g matrix –solution of the Brueckner-Bethe-Goldstone integral equation– expressed in terms of the relative momenta $\boldsymbol{\kappa}'$ and $\boldsymbol{\kappa}$ [c.f. Eqs. (3a,3b)]. The antisymmetrization of the interaction accounts for additional nonlocalities. These features have not been duly explained in previous works, leaving room for misconceptions. So it may be worth to sketch them here for clarity. To make the illustration simple let us consider the rank-0 (scalar) antisymmetrized reduced g matrix for total spin S and isospin T,

$$\langle \boldsymbol{\kappa}' \mid g^{ST} \mid \boldsymbol{\kappa} \rangle_{\mathcal{A}} = g^{ST}(\boldsymbol{\kappa}', \boldsymbol{\kappa}) - (-)^{S+T} g^{ST}(\boldsymbol{\kappa}', -\boldsymbol{\kappa}) \; .$$

Expanding in partial waves

$$g^{ST}(\boldsymbol{\kappa}', \boldsymbol{\kappa}) = \sum_{L=0} g_L^{ST}(\kappa', \kappa) \, P_L(\hat{\kappa}' \cdot \hat{\kappa}) \; ,$$

and using the property $P_L(-u) = (-)^L P_L(u)$, we can arrange the antisymmetrized g in a single sum,

$$\langle \boldsymbol{\kappa}' \mid g^{ST} \mid \boldsymbol{\kappa} \rangle_{\mathcal{A}} = \sum_{L=0} g_L^{ST}(\kappa', \kappa) \, [1 - (-)^{L+S+T}] \, P_L(\hat{\kappa}' \cdot \hat{\kappa}) \; .$$

Therefore

$$\langle \boldsymbol{\kappa}' \mid g^{ST} \mid \boldsymbol{\kappa} \rangle_{\mathcal{A}} = 2 \sum_{\text{Allowed}} g_L^{ST}(\kappa', \kappa) \, P_L(\hat{\kappa}' \cdot \hat{\kappa}) \; , \tag{13}$$

where the summation considers only those NN states allowed by the Pauli exclusion principle and the off-shell matrix elements $g_L^{ST}(\kappa', \kappa)$, direct solutions to the Brueckner-Bethe-Goldstone equation for the corresponding partial wave. In this fashion we naturally account for the knock-out exchange term.

In the case of local effective interactions [1, 17, 18], the off-shell matrix elements $g^{ST}(\boldsymbol{\kappa}', \boldsymbol{\kappa})$ are obtained *via* the Fourier transform $\tilde{v}$ of the local function $v^{ST}(r)$, hence

$$g^{ST}(\boldsymbol{\kappa}', \boldsymbol{\kappa}) = \tilde{v}^{ST}(\boldsymbol{\kappa}' - \boldsymbol{\kappa}) \; .$$

Therefore, the antisymmetrized matrix element reads

$$\langle \boldsymbol{\kappa}' \mid g^{ST} \mid \boldsymbol{\kappa} \rangle_{\mathcal{A}} = \tilde{v}^{ST}(\boldsymbol{\kappa}' - \boldsymbol{\kappa}) - (-)^{S+T} \tilde{v}^{ST}(\boldsymbol{\kappa}' + \boldsymbol{\kappa}) \; ,$$

a well known result. Here the knock-out exchange term makes the antisymmetrized interaction non local. If one uses multipole expansions to these Fourier transforms, then the antisymmetrized $\langle g^{ST} \rangle_{\mathcal{A}}$ takes the same form as that expressed by Eq. (13). In this case, however, $g_L^{ST}(\kappa', \kappa) = \int_0^\infty r^2 j_L(\kappa' r) v^{ST}(r) \, j_L(\kappa r) \, dr$.

C. The medium-dependent term

We examine more closely the structure of U_1, particularly the shape of its integrands. Since the dependence of g matrix elements on Z is set *via* the isoscalar density ρ, with $\rho = k_F^3/3\pi^2$, then we can write

$$\frac{\partial g_Z}{\partial Z} = \left(\frac{\partial g}{\partial k_F}\right)\bigg|_{k_F=\hat{k}(Z)} \hat{k}'(Z) \ ,$$

with

$$\hat{k}'(Z) = \frac{\hat{k}(Z)}{3}\frac{\partial \ln\rho}{\partial Z} \ .$$

In Fig. (1) we plot the radial dependence of the density $\rho(Z)$ (upper frame), its corresponding local Fermi momentum $\hat{k}(Z)$ (middle frame) and the negative radial derivative $-\hat{k}'(Z)$ (lower frame), for ^{16}O (solid curves) and ^{90}Zr (dashed curves), respectively. These figures exhibit clear peaks of $-\hat{k}'(Z)$ near 3 fm and 6 fm, corresponding in both cases to $\hat{k} \approx$ 0.6 fm^{-1}, *i.e.* the surface of the nucleus. We estimate in ∼3 fm the width of both peaks, limiting the region where the main contributions to U_1 should come from. The strength of these contributions are dictated by the derivative $\delta g \equiv \partial g/\partial k_F$, which depends on the energy E of the projectile.

In Fig. (2) we show the partial derivative of the on-shell g amplitude with respect to the Fermi momentum, symbolized with δg. The real and imaginary components are shown in the upper and lower frames, respectively. The left frames correspond to the pp channel, whereas the right frames correspond to the pn channel. The curves represent different projectile energies, starting at E =30 MeV (solid curves) up to 100 MeV in steps of 10 MeV (dashed curves). To facilitate their comparison, the same scale is used in all graphs. By forward (on shell) we mean $\boldsymbol{k}' = \boldsymbol{k}$, with $E = k^2/2m$, the nonrelativistic nucleon energy. Hence, $\delta g = \partial g(\boldsymbol{k}; \frac{1}{2}\boldsymbol{k}, \frac{1}{2}\boldsymbol{k})/\partial k_F$. The striking feature of this figure is the asymmetry of δg, significantly more pronounced in the pn than in the pp channel, suggesting more sensitivity to neutron densities when protons are used as projectiles. Looking at the real part of the pn coupling, the attraction is more pronounced in the region 0.2 fm$^{-1} \lesssim k_F \lesssim$ 0.6 fm^{-1}, *i.e.* the nuclear surface, a feature which diminishes with increasing energy. Regarding the imaginary contribution, the nuclear surface contributes with more absorption, whereas in the nuclear interior ($kF \gtrsim$ 0.6 fm^{-1}) it is weakened. It is important in this analysis to keep in mind that δg contributes to U_1. Instead, the leading-order contribution to the optical potential stems from U_0, which depends directly on the t matrix. To keep this observations in better perspective, in Fig. (3) we plot the forward (on shell) t matrix as function of the nucleon energy E. Here the solid and dashed curves correspond to the real and imaginary amplitude, respectively. In this figure the right-hand-side axis scales to $(2\pi)^3\,t$, to facilitate comparison with other conventional normalizations. We notice here that the absorptive component of the pn coupling exhibits a stronger energy dependence, becoming dominant as the energy decreases from $\lesssim$ 80 MeV. Instead, the real components are relatively constant throughout the energy range considered.

In order to trace the sources of the contributions to U_1 and also estimate their importance relative to U_0, we find useful to introduce the density function u_α defined by

$$u_\alpha(Z) = -\frac{Z^3}{2\pi^2}\int d\boldsymbol{P}\,\Omega_\alpha(\boldsymbol{q}=0,\boldsymbol{P};Z)\,\frac{\partial g_Z^{(0)}}{\partial Z}\;, \tag{14}$$

to be evaluated on-shell at $\boldsymbol{q}=0$ for the single-particle shell α. Its radial integral accounts for the partial contributioin U_α,

$$U_\alpha = \int_0^\infty u_\alpha(Z)\,dZ\;,$$

with $U_1=\sum_\alpha U_\alpha$. In Fig. (4) we plot the real (upper frames) and imaginary (lower frames) components of $u_\alpha(Z)$ for ^{16}O(p,p) at 30 MeV. The curves correspond to contributions from the $1p_{3/2}$ (dotted curves), $1p_{1/2}$ (dashed curves) and $1s_{1/2}$ (long-dashed curves) shells, while the solid curves represent the sum $\sum_\alpha u_\alpha^{(p,n)}$. The ($p$) and ($n$) labels symbolize contributions of the form $\langle\hat\rho_p\,\delta g_{pp}\rangle$, arising from proton densities, and $\langle\hat\rho_n\,\delta g_{pn}\rangle$ due to neutrons, respectively. Notice that the scale of *Im* u_α doubles that of *Re* u_α.

This figure evidences quite neatly surface-peaked structure stemming from δg, confined in the region 3-5.5 fm, with clear dominance of neutron over proton distributions. Considering U_0 the leading-order contribution, *Re* $u_\alpha^{(n)}$ enhances the attraction to the projectile (proton). This can be readily estimated considering its width ~1.5 fm and depth ~15 MeV fm^2. Hence, the area between the curve and the Z axis yields *Re* $U_1^{(n)}\sim$ -23 MeV fm^3. This is to be compared to $U_0^{(n)}\approx 8\times$*Re* $t_{pn}\sim$ -10 MeV fm^3, as extracted from Fig. (3). In contrast, neutron density contributions to *Im* U_1 becomes considerably weaker due to its near-canceling up-and-down structure observed in the lower-right frame, while *Im* $U_0^{(n)}\approx 8\times$*Im* $t_{pn}\sim$ -24 MeV fm^3. The extent to which these features become important in collision processes needs to be assessed by examining scattering observables. In any case, the pocket shape of *Re* $u_\alpha^{(n)}$ near the surface indicates a preference to couple the projectile (proton) with the $\nu 1p_{1/2}$ and $\nu 1p_{3/2}$ shells, favoring (p,d) pickup reactions. This feature is consistent with recent findings on pickup effects in $p+^{10}$Be elastic scattering near 40A MeV [19].

III. APPLICATIONS

We investigate proton elastic scattering from ^{16}O and ^{90}Zr, two relatively well known doubly closed-shell nuclei. In each case we consider three forms of the optical potential. First, the δg-folding approach [c.f. Eq. (11)], providing arguably the most complete momentum-space description of the optical potential to date. Here, single-particle wavefunctions are used to represent the one-body full mixed density while a thorough account of the medium dependence of the antisymmetrized off shell g matrix is given. Second, the ABL folding approach, corresponding to a simplified representation of the mixed density in terms of its Slater approximation. This approach has been extensively discussed in Refs. [9, 20]. Lastly, the free t-matrix full-folding optical potentials (t-folding), where the full mixed density is used as in the early calculations [15, 16].

The calculations presented here are based on the Paris *NN* potential [21]. We have investigated other *NN* potentials and found no significant differences with the results reported here. The corresponding g matrix was calculated off shell ($J \leq 7$) at 30 values of the Fermi momentum, ranging from 0 up to 1.6 fm^{-1}. This thin mesh is no longer necessary after various tests of convergence were performed; the use of 16 Fermi momenta yields equally reliable results. The needed selfconsistent nuclear-matter fields were computed prior to all runs.

To evaluate U_1 given by Eq. (11) we carry out the $\boldsymbol{P}$ and $\boldsymbol{Q}$ integrals using Gauss-Laguerre quadrature at 25 radial mesh points. The Z integration is performed using a uniform mesh with steps of 0.1 fm. As stated earlier, the calculated optical model potentials reported here are nonlocal operators, treated as such throughout. The scattering observables are obtained solving the Schrödinger equation with the nonlocal coupling in the presence of the Coulomb term. See Ref. [22] for more details.

A. $p+^{90}$Zr scattering

In Fig. (5) we present the measured and calculated differential cross section, as a function of the center-of-mass scattering angle $\theta_{c.m.}$, for ^{90}Zr(p,p) at 30.4 and 40 MeV. The data are from Refs. [23] and [24], respectively. The solid curves correspond to δg-folding, the dashed curves to the ABL approach and the dotted curves to the t-folding. The one-body mixed density is constructed using single-particle wavefunctions based on Hartree-Fock calculations [27].

The calculated cross sections based on the δg-folding follow reasonably well the diffractive pattern exhibited by the measurements. The maxima are in phase with the data, although the diffractive minima tend to be more pronounced. Additionally, we find that the ABL approach (dashed curves) follows very closely the δg-folding (solid curves). So, within the MCA, the ABL folding approach represents reasonably well the δg-folding. The difference lies in the computational time needed for their evaluation, being the δg-folding more time demanding (by nearly a factor 150) than its ABL counterpart.

Considering the results based on the free t matrix (dotted curves), they clearly lack the structure exhibited by the data. In particular, at the two energies considered here, the first diffractive minima occur at greater angles than those shown by the data, suggesting a smaller size nucleus. Thus, the medium effects accounted for by U_1, and located mainly in the nuclear surface, do account for some of the hadronic size of the nucleus.

As the energy increases it is expected that the medium effects become less relevant in the scattering process. This feature is clearly observed in Fig. (6), where we plot the measured and calculated differential cross section for ^{90}Zr(p,p) at 80 and 100 MeV. The data are from Refs. [25] and [26], respectively. The curves follow the same convention as in Fig, (5). The agreement of the δg-folding with the data is remarkable throughout the whole range of the measurements. Additionally, we verify that the difference between the t-folding results and those from δg- or ABL-approach have diminished considerably relative the previous applications.

B. p+^{16}O scattering

In Fig. (7) we show the measured and calculated differential cross section (upper frames) and analyzing power (lower frames), as a functions of the center-of-mass scattering angle, for ^{16}O(p,p) at 30.4 and 49.48 MeV. The cross section data are from Refs. [28] and [29], respectively. Here again we observe that the δg-folding and ABL approach follow very close each other. Also, the free t matrix results agree poorly with the data, as expected. This lighter target evidences a deviation of the calculated cross sections with the data, particularly the depth of the diffractive minima in the cross section. Indeed, both δg- and ABL-folding approaches fail to account for the shallow first minima near 40°. In turn, both yield non existing minima near 90° and 80°, respectively.

We have performed various tests of sensitivity to assess the consistency of the results presented here. For instance, using harmonic-oscillator wavefunctions for ^{16}O –with the same root-mean-squared radii– we obtain practically the same results for the scattering observables. To keep this work focused on the structure of the δg-folding, we have not explored the sensitivity of the calculated scattering to alternative representations of the target ground state, leaving such study for future works.

In Fig. (8) we examine how the differential cross section is affected upon changes on U_1. The case is ^{16}O(p,p) at 30.4 MeV. Here the solid curve represents results from the δg-folding, $U_0 + U_1$, while the dotted curve is based on U_0 alone, namely the t-folding. What is interesting to note is the effect of suppressing selectively the proton density (dash-dotted curve) and neutron density contributions to U_1 (dashed curve). We note that the role of $U_1^{(n)}$ is considerably more significant than that of $U_1^{(p)}$. Indeed, by neglecting $U_1^{(n)}$ the cross section ends up being very similar to the one obtained with the t-folding, in contrast with the moderate change on the δg-folding result when $U_1^{(p)}$ is suppressed. These results are consistent with our analysis of $u_\alpha(Z)$ discussed in the previous section, confirming the importance of neutron distributions in the optical model potential at these low energies.

IV. SUMMARY AND CONCLUSIONS

We have investigated the structure of the optical model potential as inferred from its general form, once the MCA is applied to the vector structure of the NN couplings. The resulting (δg-folding) potential becomes expressed as the sum of two components, $U_0 + U_1$, where U_0 corresponds to the free t matrix full-folding potential and U_1 folds the full mixed density with the gradient of the medium-dependent effective interaction. This feature implies that the intrinsic medium effects are localized mainly in the nuclear surface. When comparing the relative strength of these contributions, we find that the pn coupling is considerably stronger than its pp counterpart, a feature that fades out as the energy of the projectile is increased. This asymmetry leads to stronger medium-sensitivity of proton scattering to neutron matter distributions of the nucleus.

As a by product of this study, with the introduction of the δg-folding we have been able to provide a thorough account of the full mixed density in the evaluation of momentum-space optical potentials within the g matrix. With this we mend a long standing limitation of the ABL folding approach to NA scattering, where the mixed density has been approximated by its Slater form. When comparing the differential cross section, the δg-folding and ABL approach are close to one another within 10% in the diffractive maxima.

We have assessed the predicting power of the δg-folding approach to proton elastic scattering from ^{16}O and ^{90}Zr at energies between 30 and 100 MeV. In the case of ^{90}Zr(p,p) we are able to provide reasonably good descriptions of the data. For ^{16}O(p,p), in turn, the differential cross section is underestimated significantly. At this point we are not clear whether these shortcomings stem from missing contributions implied when the dependence of $\partial g/\partial Z$ on $\boldsymbol{Q}$ is neglected, the existence of exotic neutron structures in the surface, or from higher-order effects in the *in-medium* effective interaction. One has to keep in mind that the low-energy interaction of the projectile with target nucleons becomes more sensitive to the shell structure of the nucleus, in addition to the presence of collective excitations or other reaction channels. Investigations along these lines have recently been reported [19, 30].

The present work constitutes a step forward toward a comprehensive momentum-space description of the optical model potential for NA scattering, in the form of a unified description, for elastic and inelastic processes from few tens of MeV up to GeV energies. The only microscopic inputs to achieve this goal are the bare NN potential and the target ground-state mixed density, although high-energy applications may also require NN phase-shift analyzes accounting for loss of flux above pion-production threshold [20]. The introduction of the δg-folding optical potential has allowed us to visualize very simply the interplay among different elements in the interaction of a single nucleon with finite nuclei, particularly the role of the *in medium* interaction in the nuclear surface. With the application reported here we have been able to set narrower margins of uncertainty in the evaluation of the first-order optical model potential, an important consideration for high-precision analyzes of upcoming scattering data involving unstable nuclei.

Acknowledgments

H.F.A. acknowledges partial support provided by VID-UCH under grant ENL0704, and FONDECYT under grant No 1080471.

[1] K. Amos, P. J. Dortmans, H. V. von Geramb, S. Karataglidis, and J. Raynal, Adv. in Nucl. Phys. **25**, 275 (2000).

[2] L. Ray, G. W. Hoffmann and W. R. Coker, Phys. Rep. **212**, 223 (1992).

[3] H. F. Arellano and E. Bauge, Phys. Rev. C 76, 014613 (2007).

[4] See, e.g., http://www.ganil.fr/eurisol/

[5] See, e.g., http://isolde.web.cern.ch/isolde/

[6] See, e.g., http://www.ganil.fr/spiral/

[7] See, e.g., http://www.rarf.riken.go.jp/Eng/facilities/RIBF.html

[8] See, e.g., http://www.nscl.msu.edu/future/isf/

[9] H. F. Arellano, F. A. Brieva, and W. G. Love, Phys. Rev. C 52, 301 (1995).

[10] K. M. Watson, Phys. Rev. 89, 575 (1953).

[11] H. Feshbach, Ann. Phys. (N.Y.) **5**, 357 (1958); *ibid.* **19**, 287 (1962).

[12] A. K. Kerman, H. McManus, and R. M. Thaler, Ann. Phys. **8**, 551 (1959).

[13] A. L. Fetter and K. M. Watson, in *Advances in Theoretical Physics*, Vol. 1, edited by K.A. Brueckner, (Academic Press, New York, 1965)

[14] F. Villars, in *Fundamentals in Nuclear Theory*, edited by A. de-Shalit and C. Villi, (IAEA, Vienna, 1967).

[15] H. F. Arellano, F. A. Brieva, and W. G. Love, Phys. Rev. Lett. **63**, 605 (1989).

[16] H. F. Arellano, F. A. Brieva, and W. G. Love, Phys. Rev. C 41, 2188-2201 (1990)

[17] H. V. von Geramb, in *The Interaction Between Medium Energy Nucleons in Nuclei*, edited by H. O. Meyer (AIP, New York,1983).

[18] J. Raynal, computer code DWBA98 (NEA 1209/05, 1999).

[19] N. Keeley and V. Lapoux, Phys. Rev. C 77, 014605 (2008).

[20] H. F. Arellano and H. V. von Geramb, Phys. Rev. C 66, 024602 (2002).

[21] M. Lacombe, B. Loiseau, J. M. Richard, and R. Vinh Mau, J. Côté, P. Pirés and R. de Tourreil, Phys. Rev. C 21, 861 (1980).

[22] H. F. Arellano and W. G. Love Phys. Rev. C 76, 014616 (2007).

[23] R. de Swiniarski, Dinh-Lien Pham, and G. Bagieu, Can. J. Phys. 55, 43 (1977).

[24] L. N. Blumberg, E. E. Gross, A. van der Woude, A. Zucker, and R. H. Bassel, Phys. Rev. 147, 812 (1966).

[25] A. Nadasen, P. Schwandt, P. P. Singh, W. W. Jacobs, A. D. Bacher, P. T. Debevec, M. D. Kaitchuck, and J. T. Meek, Phys. Rev. C 23, 1023 (1981).

[26] K. Kwiatkowski and N. S. Wall, Nucl. Phys. A301, 349 (1978).

[27] J. W. Negele, Phys. Rev. C 1, 1260 (1970).

[28] P. D. Greaves, V. Hnizdo, J. Lowe and O. Karban, Nucl. Phys. A179, 1 (1972).

[29] J. A. Fannon, E. J. Burge, D. A. Smith and N. K. Ganguly, Nucl. Phys. A97, 263 (1967).

[30] P. Fraser, K. Amos, S. Karataglidis, L. Canton, G. Pisent and J. P. Svenne, Eur. Phys. J. A 35, 69 (2008).

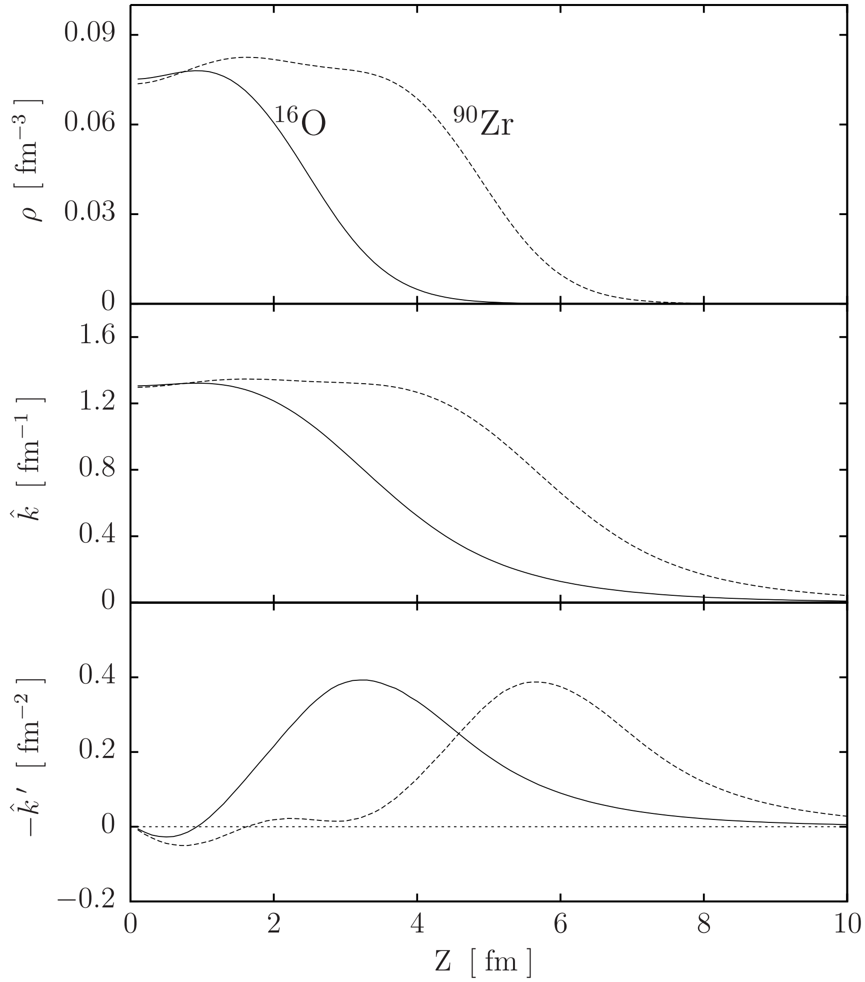

FIG. 1: Radial dependence of the density (upper frame), local Fermi momentum (middle frame) and its negative gradient (lower frame) for ^{16}O and ^{90}Zr.

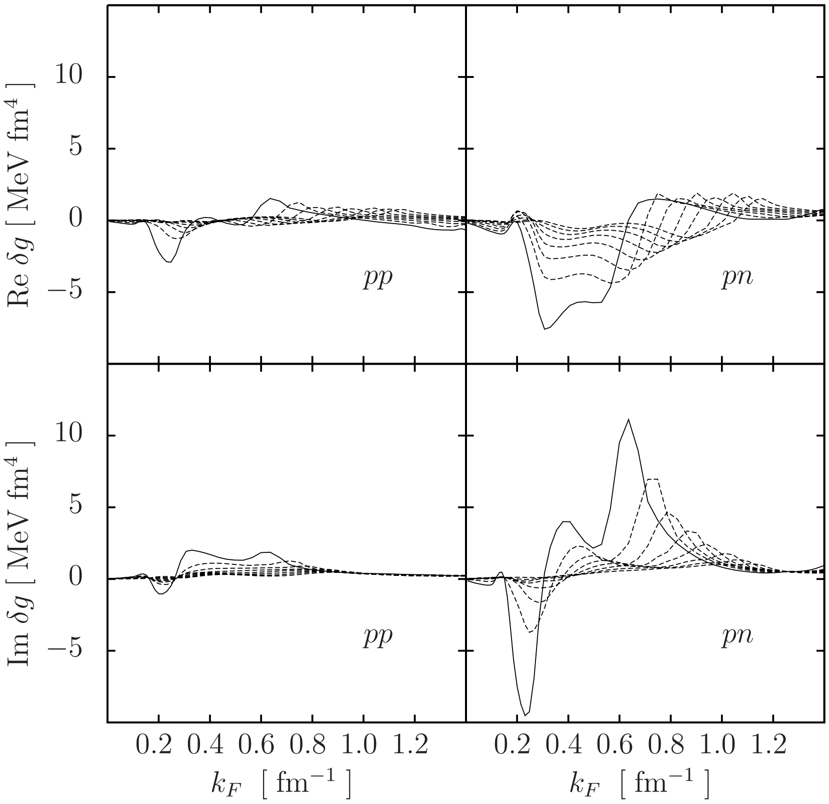

FIG. 2: Real (upper frames) and imaginary (lower frames) components of the forward $\delta g \equiv \partial g/\partial k_F$ amplitudes, in the *pp* (left frames) and *pn* (right frames) channels, as functions of the Fermi momentum. See the text for reference to the curves.

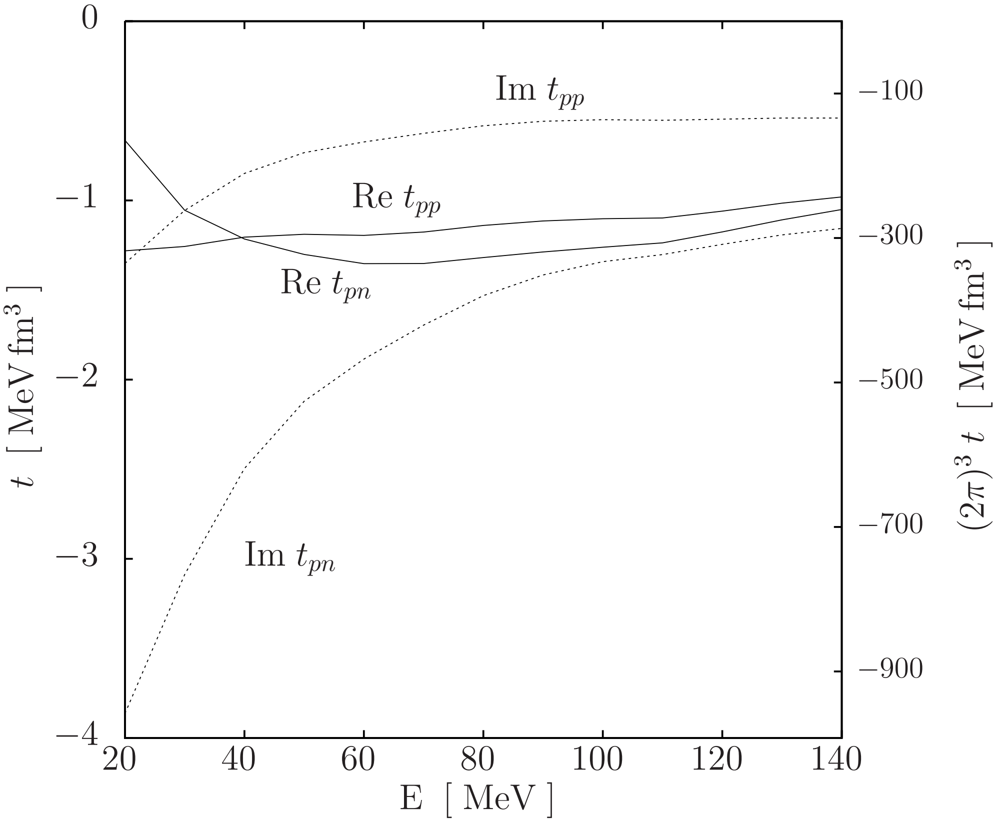

FIG. 3: Forward on-shell free t matrix as function of the nucleon energy. The solid and dashed curves correspond to the real and imaginary amplitudes, respectively.

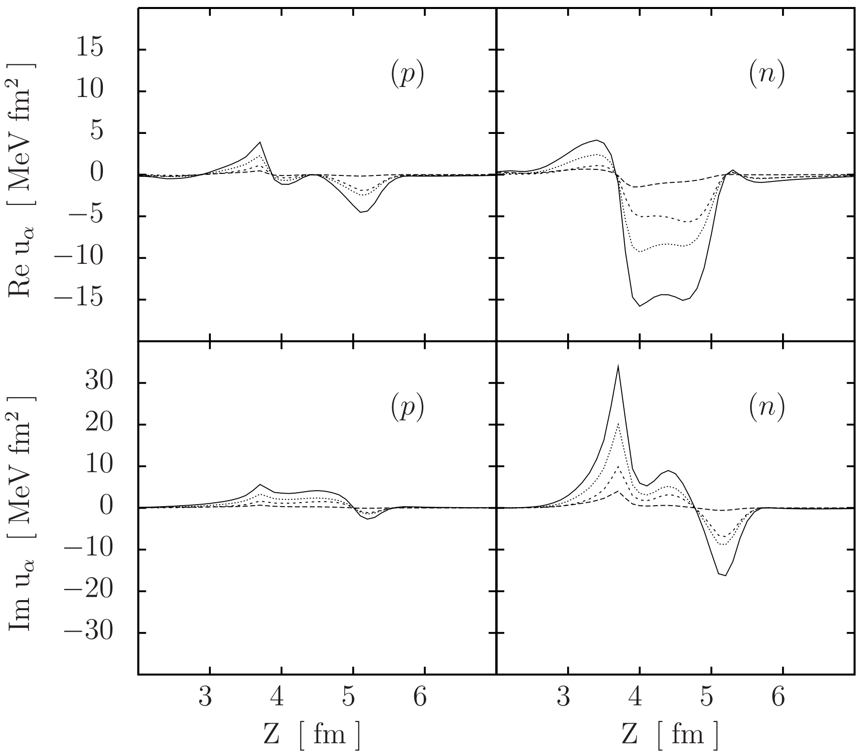

FIG. 4: The radial behavior of u_α for the pp (left frames) and pn couplings (right frame). Observe that $\sum_\alpha \int u_\alpha^{(p,n)}(Z)\,dZ = U_1^{(p,n)}$. See text for reference to the curves.

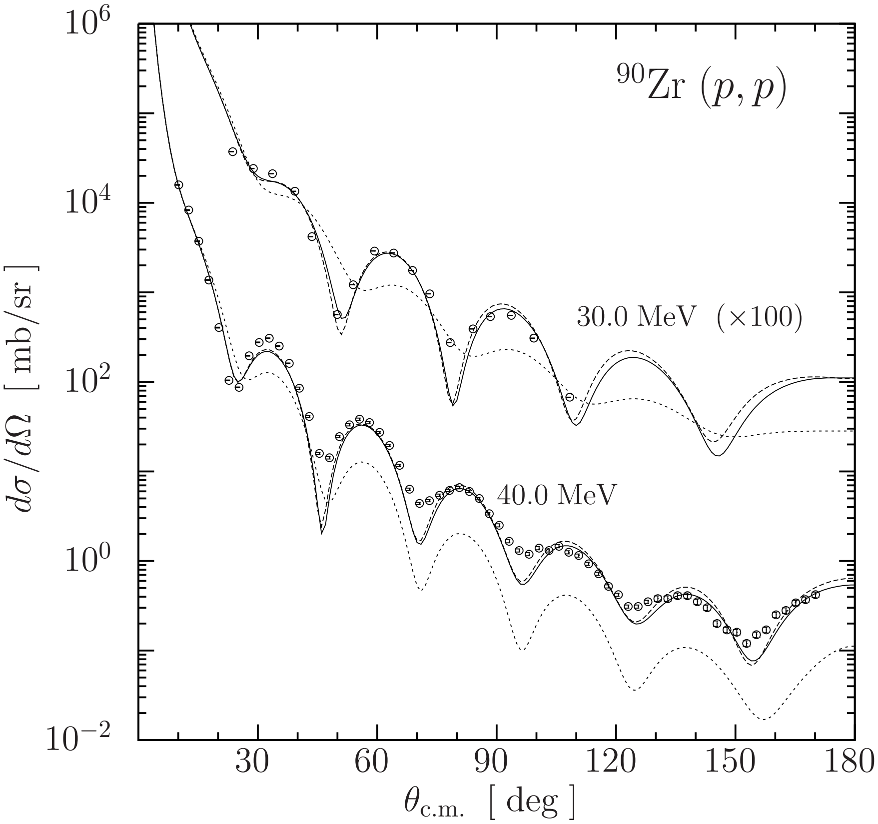

FIG. 5: The measured and calculated differential cross section for ^{90}Zr(p,p) at 30.4 and 40 MeV. The data are from Refs. [23] and [24], respectively. See text for reference to the curves.

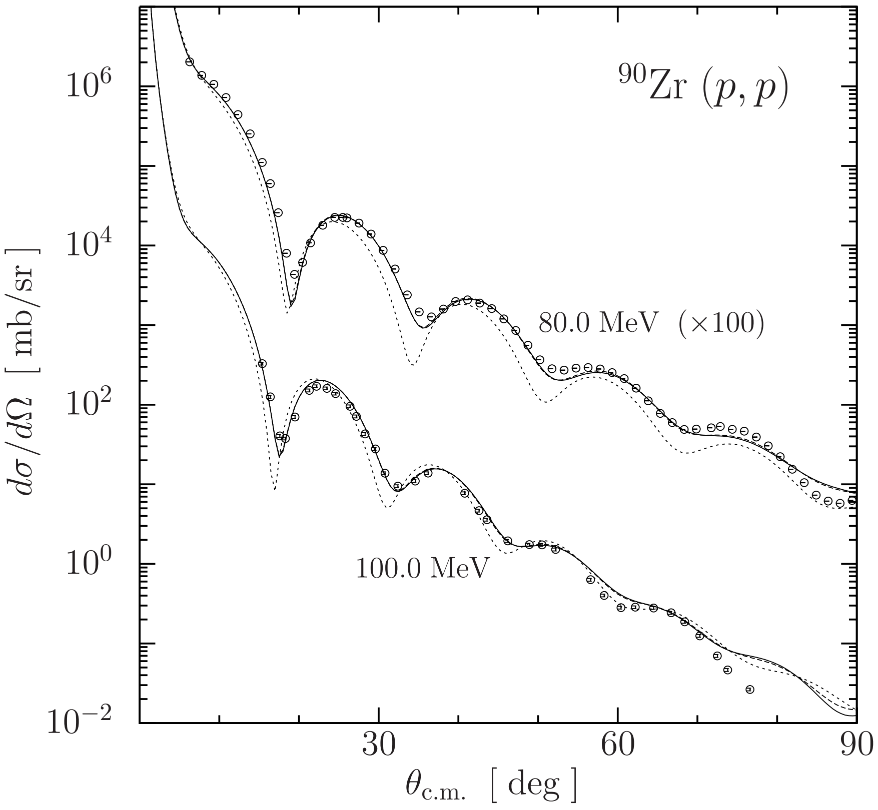

FIG. 6: The measured and calculated differential cross section for ^{90}Zr(p,p) at 80 and 100 MeV. The data are from Refs. [25] and [26], respectively. See text for reference to the curves.

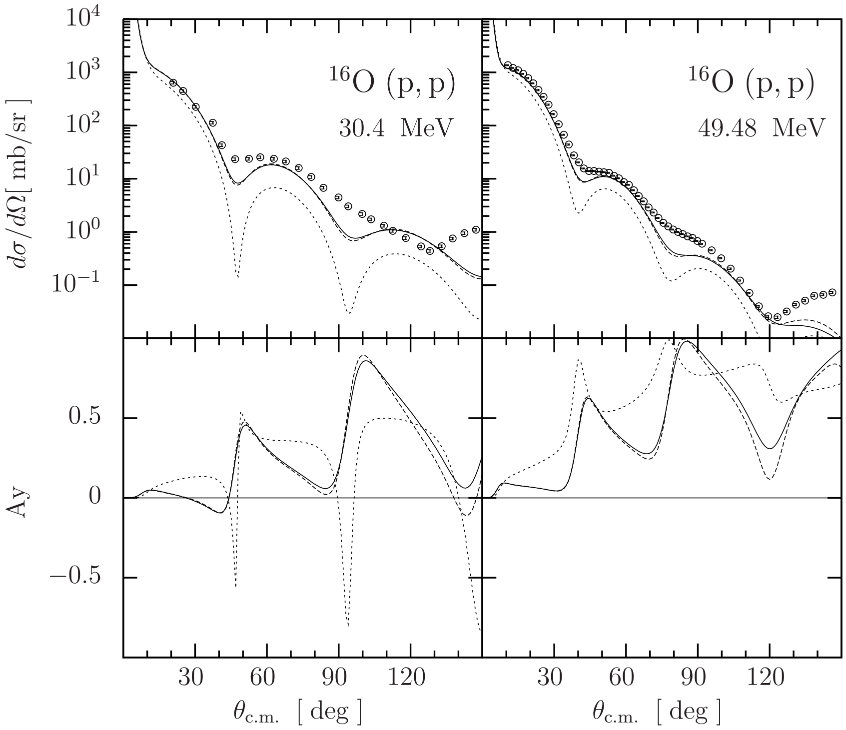

FIG. 7: Measured and calculated differential cross section for ^{16}O(p,p) at 30.4 and 49.48 MeV (upper frames), and calculated analyzing power (lower frames). The data are from Refs. [28] and [29], respectively. See text for reference to the curves.

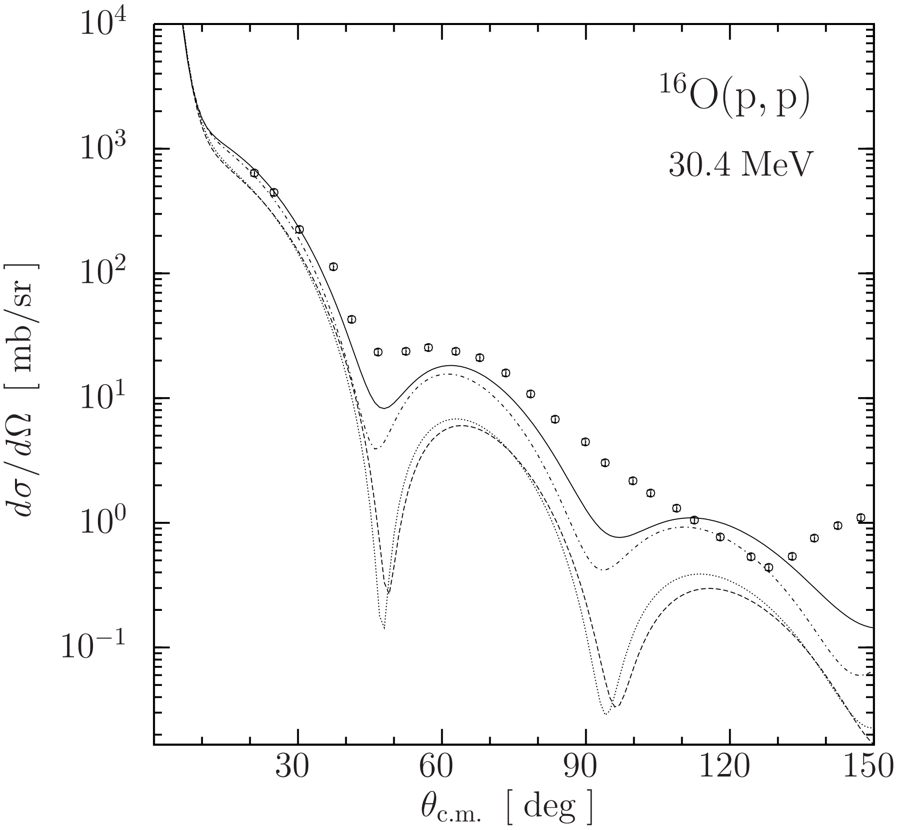

FIG. 8: The calculated differential cross section based on the δg-folding (solid curve) and t-folding (dotted curve) for ^{16}O(p,p) scattering at 30.4 MeV. The data are from [28]. See text for reference to the dashed curves.